



Rationale design of a layer-by-layer nanostructure for X-ray induced photodynamic therapy

Davide Orsi^a, Davide Bernardi^a, Guglielmo Giovanardi^a, Francesca Rossi^b,
Krzysztof Szczepanowicz^c, Luigi Cristofolini^{a,*}

^a Department of Mathematical, Physical and Computer Sciences, University of Parma, Italy

^b Istituto dei Materiali per l'Elettronica ed il Magnetismo, Consiglio Nazionale delle Ricerche, Parma, Italy

^c Jerzy Haber Institute of Catalysis and Surface Chemistry, Polish Academy of Sciences, Krakow, Poland

ABSTRACT

X-ray induced Photodynamic Therapy (XPDT) is a proposed therapy for deep tumours. The idea is to use the X-ray beam of a standard radiotherapy facility to excite a scintillator which is coupled with a photosensitizing agent which in turn generates reactive oxygen species (ROS) which induce local oxidative stress. Alike in standard Photodynamic Therapy, this oxidative stress may be used to treat tumours. Preliminary results [F. Rossi et al. Sci. Rep. 5 (2015) 7606] demonstrated that can XPDT enhance the efficacy of standard radiotherapy, while reducing its unwanted side effects.

This work reports the rationale development of a nanostructure incorporating nanoparticles (NP) for XPDT around a silica core by means of electrostatic adsorption. To this aim, scintillator CeF₃ and photosensitizer ZnO, both in form of nanoparticles, have been adsorbed into a polyelectrolyte Layer-by-Layer (LbL) multilayer grown around a SiO₂ core. This structure, in a future work, could be a platform for drug delivery.

We optimized the growth of the structure basing on results from adsorption on planar substrates, as a function of incubation time, of particle concentration, and of the composition of the outer polyelectrolyte layer, having also in mind the need to avoid the formation of micrometric aggregates. This drove the rationale synthesis of the nanocapsules. The resulting structures are studied by Scanning Electron Microscopy, X-ray Microanalysis, Dynamic Light Scattering, and ζ -potential analysis.

1. Introduction

Chemotherapy and Radiotherapy are typically combined to treat deep or metastatic tumours. Both therapies might present severe side effects that impact on the patients' health and quality of life. In the case of systemic chemotherapy, its well-known severe side effects are coupled with the possible onset of chemoresistance. In Radiotherapy, the whole X-ray beam travel path across the body is affected, including healthy tissue. Several irradiation strategies have been developed to minimize the dose received by healthy tissues and organs in proximity of the tumour, such as Volumetric Modulated Arc Therapy; there, a continuous rotation of the radiation source allows the patient to be treated from a full 360° beam angle, delivering a dose whose distribution is highly conformal to the tumour volume [1,2].

Nanostructure-based therapies are widely studied as coadjutors of standard therapies, often combining different therapeutic approaches to induce cancer cell death, improving the overall efficacy beyond the limits of each individual therapy [3,4]. Such is the case, for instance, of nanocapsules for combined magnetic hyperthermia and drug delivery [5–8], or nanostructures combining drug delivery with Photodynamic

Therapy (PDT) [9–11].

Another class of nanostructure-based approaches to cancer therapy is Self-Lighted Photodynamic Therapy (SLPDT), where a nanostructure acts a localized nano-source of light for PDT, reaching tissues not accessible by visible-NIR light of limited penetration depth. For instance, X-ray induced Photodynamic Therapy (XPDT) nanostructures combines a scintillating nanomaterial (the localized light source, triggered by a Radiotherapy X-ray beam) and a photosensitizer molecule/nanomaterial. The scintillator acts as an energy mediator, transferring energy from the flux generated by the high energy X-rays, to the photosensitizing agent that generates reactive oxygen species (ROS) which damage cancer cells by oxidative stress.

Since the first exploration of the XPDT concept by W. Chen in 2006 [12], a wide range of XPDT nanostructures have been investigated, combining scintillating nanostructures of different shape and size with organic and inorganic photosensitizers [13–16]. Notably, cytocompatible inorganic SiC/SiO_x core/shell nanowires conjugated with an organic photosensitizer, excited at low dose (≤ 2 Gy) by a clinical source of X rays at 6 MeV, demonstrated high efficiency against human lung adenocarcinoma cells (A549) with a reduction with respect to control of

* Corresponding author.

E-mail address: luigi.cristofolini@unipr.it (L. Cristofolini).

about 75% in 12 days [17]. To overcome the limitations inherent to the relatively large size in one dimension of nanowires, we recently synthesized and characterized the XPDT performances of composite nanostructures combining CeF_3 and ZnO [18,19]. The former is an efficient scintillator, with a broad emission band at 300 nm, while the latter is a well-known photosensitizer material that absorbs UV light below 350 nm to generate ROS; their combination is known to result in efficient X-ray induced ROS generation [20]. Our CeF_3 -ZnO nanostructures were shown to be effective XPDT agents, reducing viability of A549 cells by 18% more than the sum of X-ray irradiation and nanostructure activity without irradiation [19]. These works contribute to a growing interest in the combined use of lanthanide-fluorides nanoscintillators and photosensitizing ZnO nanocrystals for XPDT applied to deep tumours [14,21,22].

This work develops a rationale design of a nanostructure, built around an amorphous SiO_2 nanoparticle template, that incorporates XPDT nanoparticles (NP) of these materials, CeF_3 and ZnO, within a polyelectrolyte Layer-by-Layer (LbL) shell. Three objectives guided us:

- 1) to obtain nanostructure with a narrow size distribution, and with constant ratio of CeF_3 and ZnO
- 2) to avoid letting either ZnO or CeF_3 NP as isolated nanoparticles in the suspension
- 3) to avoid formation of larger (micrometric) aggregates in the suspension.

The LbL technique grants a precise control on the structure of the resulting nanostructure, obtained by tuning the adsorption conditions in each successive layer deposition [23,24]; the three goals stated above have been pursued through a detailed investigation of the effects on NP adsorption of several physico-chemical parameters, such as ionic strength, polyelectrolyte concentration, incubation time [25].

SiO_2 -based nanostructures have been proposed as ideal platforms to combine PDT and drug delivery [9,11,26]. The sol-gel synthesis ensures monodisperse size in the range 50-500 nm. Mesoporous silica NP are used as a platform for pH-responsive drug delivery, releasing the cargo upon reaching low pH environments, typical of several tumours [27]. The use of the Layer-by-Layer technique to assemble a mixed NP-polyelectrolyte shell around a larger nanoparticle core was pioneered in 1999 by Caruso and Möhwald [28]; they assembled monodisperse silica NP on larger polystyrene cores with poly(diallyldimethylammonium chloride) (PDADMAC) as polyelectrolyte. Afterwards, many applications of nanoparticle-on-nanoparticle LbL structures were published, with among others TiO_2 , Fe_3O_4 , SiO_2 , Au NP assembled around solid cores [29,30].

The rest of the works is structured as follows. First, we report on the morphological characterization of the ZnO and CeF_3 NP and of the SiO_2 cores. Next, we describe the structure of the polyelectrolyte LbL multilayer and discuss the maximum adsorption density of ZnO and CeF_3 NP onto its surface. This is done in planar geometry, because it allows investigation by Scanning Electron Microscopy (SEM) and null-ellipsometry.

The information on the adsorption density was used to determine the ideal conditions for the self-assembly of the LbL nanostructures, in terms of concentrations and incubation times. The structure of the CeF_3 -ZnO- SiO_2 LbL assemblies was characterized by Dynamic Light Scattering (DLS), SEM, ζ -potential analysis; the presence of XPDT NP within the LbL shell was confirmed combining Energy Dispersive X-ray (EDX) Microanalysis and Fluorescence spectroscopy. Finally, the potential of the combination of CeF_3 and ZnO nanoparticles for XPDT, already well known from the literature, is assessed by measuring the singlet oxygen quantum yield under UV irradiation.

2. Materials and methods

Polystyrene sulfonate (PSS, Sigma Aldrich, M.W. 70,000, CAS

25704-18-1), Poly(diallyldimethylammonium chloride) solution (PDADMAC, Sigma Aldrich, 20% wt solution, CAS 26062-79-3) and Polyethyleneimine (PEI, Sigma Aldrich, 50% w/v solution, CAS 9002-98-6) solutions were prepared in ultrapure water (Milli-Q water purification system, Millipore Corporation, resistivity 18.2 M Ω) or in 15 mM NaCl solution.

Cerium nitrate hexahydrate (>99% purity CAS 10294-41-4), Sodium hydroxide anhydrous (>98%, pellets, CAS 1310-73-2), Ammonium fluoride (CAS 12125-01-8), Zinc Acetate dihydrate (>99%, CAS 5970-45-6), and Tetraethyl orthosilicate (TEOS, >99%, CAS 78-10-4) were purchased from Sigma Aldrich and used as received. Ammonia solution (38% w/v), Methanol and Ethylene glycol (99% purity) were purchased from Carlo Erba Reagents S.r.l.

2.1. Synthesis of SiO_2 nanoparticles

Amorphous SiO_2 nanoparticles were synthesized with the Stöber process, following ref. [31]. Briefly, a 0.17 M TEOS solution in methanol (245 mL) was put in a 500 mL beaker under magnetic stirring at 300 rpm, and heated to 65 °C. Then, 13.4 g of ammonia solution (38% w/v) and 40.6 g of water were rapidly added during stirring, reaching 1 M ammonia concentration and 10 M ammonia concentration in the resulting solution. The sample was left stirring for three hours. The NP were collected by centrifugation and washed in ultrapure water. The suspension was stored in a glass vial and sonicated prior to use.

2.2. Synthesis of CeF_3 nanoparticles

Synthesis of CeF_3 NP was performed following the procedure detailed in ref. [32]. A solution of cerium nitrate in ethylene glycol (0.6 mmol in 9 mL) was placed in a round two-way flask connected to a condenser column. 300 mg of polyethyleneimine (PEI) aqueous solution 50% wt were added. The flask was placed in an oil bath and the solution heated to 120 °C for 30 min under magnetic stirring at 300 rpm, in nitrogen atmosphere, to completely remove water from the glycol solution. Then, a solution of Ammonium fluoride in ethylene glycol (1.8 mmol in 6 mL) was added drop by drop. Then, the solution was heated to the glycol boiling point (198 °C) for 2 h, in nitrogen atmosphere, with magnetic stirring at 300 rpm.

The white precipitate was collected and washed in isopropanol by centrifugation at 13000 rpm for 15 min; the cleaning procedure was repeated 3 times.

The NP were dispersed in water, sonicated in ultrasonic bath for 10 min, and left for 1 night to sediment; the sediment was discarded. The suspension was centrifuged at 2000 g for 8 min, to remove the fraction of larger particles; the supernatant suspension was collected in a glass vial.

2.3. Synthesis of ZnO nanoparticles

The synthesis of ZnO NP was performed in ethanol at low temperature. 2 mmol of Zinc Acetate dihydrate were dispersed in 5 mL ethanol. The solution was placed in a 20 mL beaker and heated to 65 °C while stirring at 200 rpm. After temperature stabilization, 5 mL ethanol containing 3.5 mmol of KOH were added in the beaker. A white precipitate was formed; the suspension was left cooling while stirring. Then, the particulate was collected by centrifugation and washed in water. The suspension was then centrifuged at 2000 g for 8 min, to remove the fraction of larger particles; the supernatant suspension was collected in a glass vial.

2.4. Characterization of the silica cores and of the other nanoparticles to be subsequently assembled around them

SiO_2 cores, also after the growth of Layer-by-Layer structures, as well as CeF_3 and ZnO NPs, have all been characterized combining DLS, Electrophoresis for ζ -potential analysis, SEM, Energy Dispersive X-ray

(EDS) spectroscopy, and Fluorescence spectroscopy. DLS was performed on a Brookhaven 90plus operating with 90° scattering angle and a 658 nm solid state laser. Electrophoresis for ζ -potential analysis was performed on the same instrument, averaging over 10 repetitions. Samples were contained in standard polycarbonate cuvettes (vol. $1\text{ cm} \times 1\text{ cm} \times 4\text{ cm}$). SiO_2 NP size distribution have average diameter 420 nm with standard deviation of 42 nm; their ζ -potential is $-58 \pm 1\text{ mV}$. CeF_3 NP size distribution have average diameter 47 nm with standard deviation of 11 nm; their ζ -potential is $+53 \pm 1\text{ mV}$. ZnO NP size distribution have average diameter 49 nm with standard deviation of 17 nm; their ζ -potential is $+53 \pm 3\text{ mV}$. Size distributions of CeF_3 and ZnO nanoparticles, measured by DLS and SEM, are reported as supplementary information.

SEM analyses were performed using a Field-Emission SUPRA40 Zeiss SEM equipped with a GEMINI FESEM detection column; an Oxford instruments EDX microanalysis setup was used for elemental analysis of nanostructures.

Fluorescence spectra were acquired using a Jasco FP-550 spectrofluorometer; the samples were contained in standard quartz cuvettes, with volume $1\text{ cm} \times 1\text{ cm} \times 4\text{ cm}$.

SEM was also used to determine the concentration of NP in suspension. A drop of suspension of known volume is left to dry on a Silicon wafer, treated to be highly Hydrophilic with a piranha solution to minimize coffee-ring effects. By evaluating the surface density of NP, an estimate of the NP-per-unit-volume concentration is obtained. For consistency, this value is checked from that derived from the weight concentration of NP in suspension, knowing the average particle size.

Phase purity was also checked by High Resolution Transmission Electron Microscopy. The crystalline structure of the ZnO and CeF_3 nanomaterials, deposited by drop casting on Carbon coated Copper grids, was analysed by Transmission Electron Microscopy in a JEOL JEM 2200 FS microscope operated at 200 kV.

2.5. Electrostatic adsorption on planar substrate

The design of the LbL nanostructures was optimized basing on investigations on planar substrates, which allow detailed characterizations of the growth process [33,34]. As planar substrates, we employed Si wafers covered by natural oxide and cut into chips of $\sim 2 - 3\text{ cm}^2$. Right before use, each chip was cleaned and made highly hydrophilic by immersion in piranha solution (H_2SO_4 95% mixed with H_2O_2 36 volumes solution, ratio 3:1) for 1 h; then, it was washed with ultrapure water. This substrate was immersed in the desired polyelectrolyte solution for 15 min, followed by 5 min immersion in water. During immersion, the beaker with the solution was placed on an oscillating table operating at 0.5 Hz. After immersion in water, the assembly was dried with nitrogen and then characterized by null-ellipsometry. The procedure was repeated, alternating polyelectrolytes, until the desired number of layers was assembled.

2.6. Ellipsometric characterization of the thickness of films on planar substrates

The thickness of each constituent of the multilayer assembly was measured incrementally after each step of adsorption by null-ellipsometry [34], using an ellipsometer (Multiskop, Optrel GbR) operating with a He—Ne laser (633 nm) [35]. The angle of incidence was set to 70° and measured accurately against a standard reference. The thickness of the silicon oxide layer was measured on each chip, after piranha cleaning and just prior to the film growth steps. At least 4 different spots where measured and averaged at each step of film growth. Under the Drude approximation, which holds valid for such thin films, the film thickness is directly proportional to the change in the ellipsometric angle Δ . The conversion factor depends on the refractive index of the film, for which in this work we assumed an average value $n = 1.50$.

2.7. XPDT nanoparticle adsorption on SiO_2 nanoparticles

SiO_2 NP were incubated in polyelectrolyte solutions prepared with 15 mM NaCl. Polyelectrolyte concentration ranged between 0.2 g/L and 2 g/L; the concentration values for each LbL layer are detailed in Section 3.2. Incubation lasted for 30 min, while stirring with a magnetic agitator. At the start of the process, the concentration of SiO_2 NP is $10^{10} \frac{\text{part}}{\text{mL}}$. After each cycle of adsorption, SiO_2 NP were collected by mild centrifugation (5000 rpm, 4 min) and washed two times in 15 mM NaCl solution. An aliquot of the suspension is diluted 1:50 in 15 mM NaCl and placed in plastic cuvette for DLS and ζ -potential analysis.

CeF_3 NP and ZnO NP electrostatic adsorption on spherical LbL assemblies is performed following an analogous procedure. A precise amount of CeF_3/ZnO NP suspension of known concentration is added to the LbL assembly suspension, reaching the desired NP/core ratio; the suspension is incubated for 1 h with magnetic stirring. In this case, no washing procedure is performed, as no excess of CeF_3/ZnO NP is foreseen; the NP/core ratio is chosen to be below the expected maximum adsorption threshold determined by the preliminary study of adsorption on planar substrate.

2.8. Measurement of the $^1\text{O}_2$ quantum yield

The $^1\text{O}_2$ quantum yield of a CeF_3 - ZnO nanoparticle suspensions (50 $\mu\text{g}/\text{mL}$ concentration) was measured using the chemiluminescent probe Singlet Oxygen Sensor Green (SOSG) under irradiation with 254 nm UV light (UVGL-15 UV lamp from Analytik Jena); the measurement followed a methodology detailed in [19,36]. SOSG is a selective, quantitative probe for $^1\text{O}_2$; the fluorescence intensity of a SOSG solution is proportional to the amount of generated $^1\text{O}_2$.

The CeF_3 - ZnO nanoparticle suspension with 5 $\mu\text{g}/\text{mL}$ SOSG is placed in a quartz cuvette and irradiated with UV light, and SOSG fluorescence is measured as a function of time. SOSG fluorescence is measured using a Perkin-Elmer LS50 spectrometer with excitation at 488 nm and emission measured in the range of 510–610 nm. A measurement from a SOSG solution without nanoparticles is used as background, to account for SOSG activation from UV irradiation. A reference measurement with methylene blue, a well-known organic photosensitizer with quantum yield $\Phi_{\text{MB}} = 0.5$, is used to obtain the conversion from SOSG fluorescence intensity to number of $^1\text{O}_2$ generated molecules.

3. Results and discussion

3.1. Towards a rationale design: determining the maximum density of adsorbed nanoparticles

Aiming at rational design of the LbL nanostructures, the starting step was to determine the structure of the polymeric layers, and how this influences the density of CeF_3 NP that can adsorb per unit area. This investigation can be carried out much more accurately on planar substrates, than around curved surfaces. In planar geometry, ellipsometry can be applied to determine film thickness with nominal sub-angstrom accuracy, while SEM investigation allows to correlate with adsorbed particle density with no shadowed areas, as it would be for structures grown around a spherical core.

Using these techniques, we studied the effects of growth parameters such as polyelectrolyte and NP concentration and incubation time. The information thus obtained is then used for the rationale design of the nanostructures grown around the SiO_2 spherical cores.

On planar silicon chips, the first adsorbed layer is PEI; then PSS and PDADMAC layers are alternated, ending with PSS. Fig. 1 reports the null-ellipsometry thickness of the sample as a function of the number of adsorbed layers.

We found that increasing the number of layers beyond 4 led to higher inhomogeneity of the sample surface; in the adsorption onto SiO_2 NP the

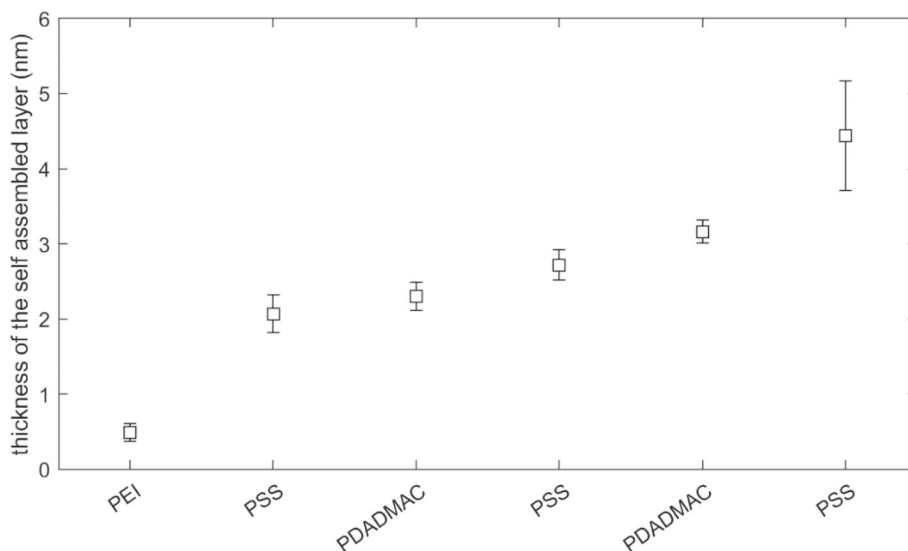


Fig. 1. Null-ellipsometry measurement of thickness of self-assembled layers prepared with polyelectrolyte concentration 0.5 g/L, as a function of the polyelectrolyte layer indicated in the abscissae axis. Error bars are standard deviation of the results from several samples, with multiple measurement points on each sample.

number of LbL layers was limited to 4, ending with a PSS layer.

Then, the LbL assembly was immersed in the CeF_3 nanoparticle suspension, with concentrations $[\text{CeF}_3]$ in the range $1 \cdot 10^{11} - 5 \cdot 10^{12} \frac{\text{part}}{\text{mL}}$, for a time ranging from 5 min to several hours. SEM imaging was used to characterize the surface adsorption of CeF_3 NP. A summary of the results is reported in Fig. 2. Panels a) - c) report SEM micrograph of three different multilayer assemblies, with contrast maximized to enhance NP visibility; these samples were prepared with $[\text{CeF}_3] = 10^{12} \frac{\text{part}}{\text{mL}}$ for three different values of [PSS], 0.2 g/L (panel a), 0.5 g/L (panel b) and 2 g/L (panel c).

The bottom panel reports the CeF_3 particle density on LbL multilayers, as a function of incubation time, for several values of $[\text{CeF}_3]$ and [PSS]. Particle density was evaluated by analysis of SEM images with the ImageJ software; it is calculated as the inverse of the area of Voronoi tessellation build from particle positions [37,38] (details reported as supplementary information). Points report the mode of particle density distributions (reported as supplementary information, fig. S1), error bars are HWHM.

The density of adsorbed NP increases with [PSS]. One possible explanation could be that the adsorbed layer is incomplete. The effect of incubation time with CeF_3 NP was investigated, varying it from 5 min up to 15 h; saturation of the adsorption density was already reached in 20 min (all the details are reported in the Supplementary Information section).

Having excluded incomplete adsorption as explanation of the limited surface coverage, we suppose that the reason for the observed increase of adsorbed NP as a function of PSS concentration in solution is to be ascribed to different conformations of the adsorbed polyelectrolyte chains. It is reasonable to expect that with increasing concentration in solution, the surface is covered by polyelectrolyte chains only partly adhering the surface, with more and more dangling chains of PSS protruding into the liquid phase. These in turn can capture an increasing number of NP. This is also consistent with the observed large thickness of the first PSS layers, as shown in Fig. 1.

By choosing $[\text{PSS}] = 0.5 \text{ g/L}$ for the outer polyelectrolyte layer, we obtain an average of 22 ± 14 CeF_3 NP per micron squared. By choosing $[\text{PSS}] = 2 \text{ g/L}$ for the outer polyelectrolyte layer, we obtain an average of 50 ± 25 CeF_3 NP per micron squared. On average, a SiO_2 core nanoparticle has a surface $S = 0.55 \pm 0.11 \mu\text{m}^2$.

Thus, in the following experiments on LbL adsorption on SiO_2 NPs, a $\text{CeF}_3:\text{SiO}_2$ ratio of 20:1 was used, with the objective of reaching the maximum CeF_3 coverage allowed with minimal free CeF_3 NP in the

suspension. We tested this on LbL layers where the final PSS layer was formed with two values of [PSS] used for the last LbL layer, 0.5 g/L and 2 g/L. It is worth noting that the maximum fraction of covered surface is $\Phi = 6.3\%$, observed for the sample with $[\text{PSS}] = 2 \text{ g/L}$.

3.2. Stoichiometric adsorption of CeF_3 NP around spherical SiO_2 cores

Building on the information thus obtained, we investigated the possibility of reaching a complete, stoichiometric adsorption of SLPD NP around the template cores. The aim is to minimize the amount of free XPDT NP in the suspension, without having to rely on centrifugation procedures for their elimination. In fact, centrifugation separation of XPDT NP and SiO_2 cores is challenging because of their small difference in size.

The starting concentration of SiO_2 NP was $10^{10} \frac{\text{part}}{\text{mL}}$. The adsorption of CeF_3 NP on SiO_2 NP was performed on assemblies prepared with 4 LbL polyelectrolyte layers. In order from inner layer to outer layer: $[\text{PDADMAC}] = 0.5 \text{ g/L}$, $[\text{PSS}] = 0.5 \text{ g/L}$, $[\text{PDADMAC}] = 0.5 \text{ g/L}$. We tested two concentrations of the fourth layer: $[\text{PSS}] = 0.5 \text{ g/L}$ and $[\text{PSS}] = 2 \text{ g/L}$. In all cases, the polyelectrolyte solutions contained 15 mM NaCl. At such low ionic strength conditions and polyelectrolyte concentrations, the multilayer thickness increases following a linear growth regime [39]. The incubation time of 30 min used throughout all the adsorption steps is much larger than the adsorption time τ_1 of PDADMAC and PSS, which describes the transport at the interface and the adsorption though the electrostatic barrier, and larger or comparable to the reorganization time τ_2 of the polymeric chains within the last adsorbed layer and the multilayer [39,40]. Thus, kinetic effects on the adsorption process and incomplete layer formation are excluded.

Small volumes of CeF_3 suspensions of known concentration were added to batches of the SiO_2 suspension, to reach two values of $\text{CeF}_3:\text{SiO}_2$ ratio: 20:1 and 50:1. The 20:1 ratio corresponds to a slight excess with respect to the average adsorption density for $[\text{PSS}] = 0.5 \text{ g/L}$ as reported in the previous section; the 50:1 ratio corresponds to a slight excess with respect to the average adsorption density for $[\text{PSS}] = 2.0 \text{ g/L}$.

To check for the adsorption of polyelectrolytes and CeF_3 NP, we performed Dynamic Light Scattering and ζ -potential measurements by electrophoresis. Results for a sample with $[\text{PSS}] = 2 \text{ g/L}$ in the fourth layer and $\text{CeF}_3:\text{SiO}_2$ ratio of 50:1 are reported in Fig. 3; analogous results have been obtained for all samples.

We note that, after the adsorption of CeF_3 NP, no washing step is

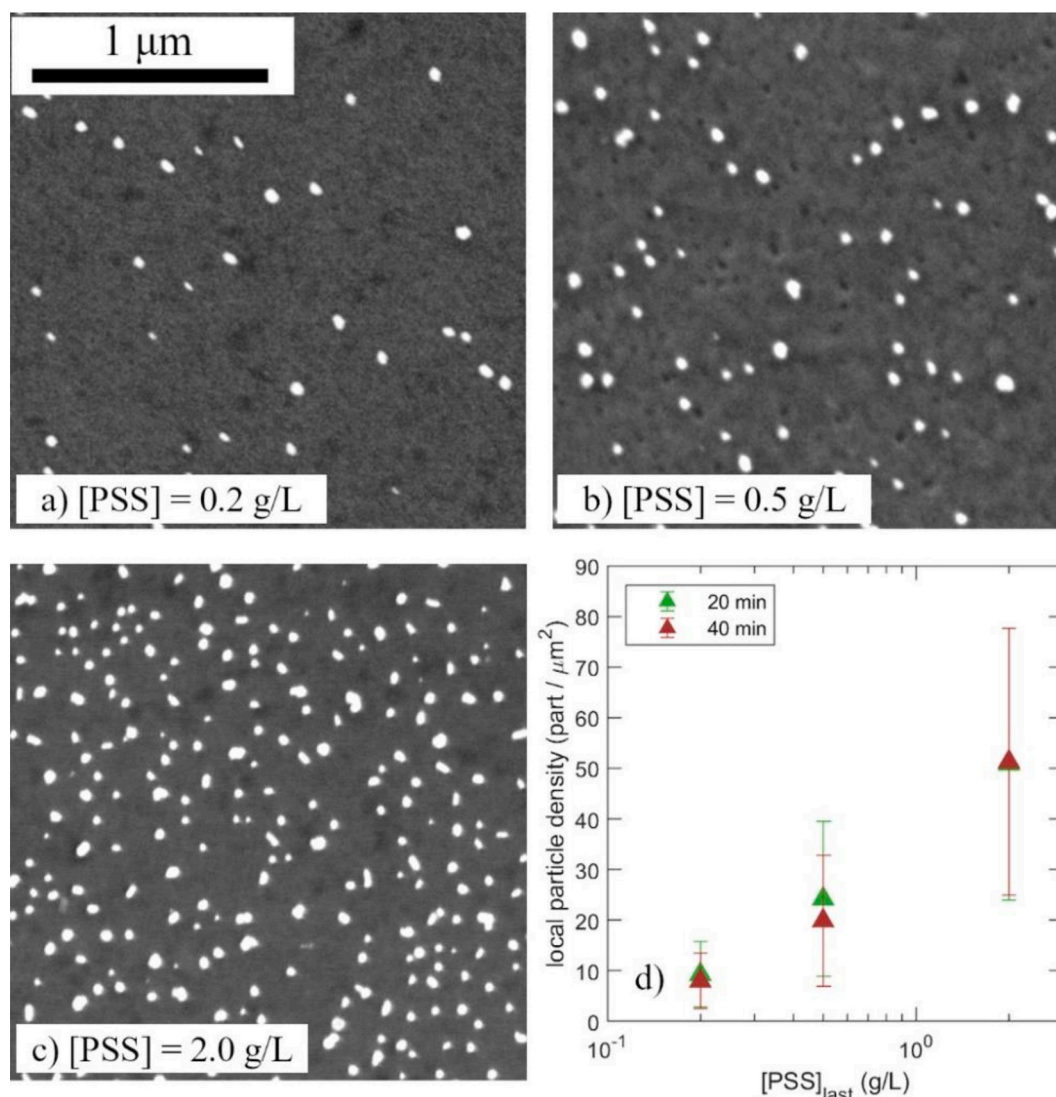


Fig. 2. SEM micrographs of CeF₃ NP adsorbed on a LbL polyelectrolyte multilayer on silicon wafer. Polyelectrolyte multilayers were incubated in CeF₃ NP suspension of concentration 10¹² part/mL for 40 min. Panels a-c report samples with three value of [PSS] used for the assembly of the last LbL layer, 0.2 g/L (a), 0.5 g/L (b) and 2 g/L (c). d) CeF₃ particle density on LbL multilayers, as a function of [PSS] used for the last layer. Varying NP incubation times yields the same results (see SI). Particle density was evaluated by analysis of SEM images with the ImageJ software, as the inverse of the area of Voronoi tessellation build from particle positions. Points report the mode of particle density distributions (reported as Supplementary Information, fig. S2), error bars are HWHM.

performed, as we expect the majority of NP to adsorb onto the SiO₂ NP surface.

The size distribution was obtained by an analysis using the CONTIN algorithm; its regularization parameter was chosen as the maximum value that did not increase the reduced χ^2 of the fit. The average size of the volume-weighted distribution shows a shift of the distribution of ~150 nm towards larger size, with only a minor growth of the distribution Full Width at Half Maximum. This is compatible with the adsorption of CeF₃ NP on the surface of the LbL assembly; the increase in width is also due to the formation of a minority fraction of dimers and trimers of SiO₂ NP, whose presence has been confirmed by SEM imaging. On the contrary, CeF₃ aggregates with size comparable to SiO₂ NP have not been observed.

The ζ -potential increases slightly after CeF₃ NP adsorption, from the value measured for the previous PSS layer; however, it remains very distant with respect to ζ -potential value of bare CeF₃ NP, +53 mV, that would indicate the formation of a dense layer of CeF₃ NP. This confirms the partial coverage of CeF₃ NP around the core, expected from the preliminary investigation in planar geometry. In those experiments, reported in Section 3.1, LbL adsorption in presence of a large excess of

CeF₃ NP never resulted in a complete layer of CeF₃ NP, even with adsorption times of several hours (see, supplementary information). The maximum value of average fraction of NP-covered surface was 6.3%, observed in the case of [PSS] = 2 g/L.

SEM imaging provides detailed insight on the adsorption of CeF₃ NP. Samples were prepared by as follows: a silicon substrate covered by a LbL layer of PDADMAC, prepared with a procedure analogous to that reported in Section 2.3, was immersed in a suspension of SiO₂-CeF₃ assemblies, diluted 50 times in ultrapure water. SEM imaging results are reported in Fig. 4 as a function of [PSS] and [CeF₃] concentrations. Images of the LbL assemblies (Fig. 4) confirms the incomplete surface coverage of CeF₃ NP around the SiO₂ core suggested by ζ -potential measurements.

Fig. 4 reports histograms of the number of CeF₃ NP counted on the visible half of SiO₂-CeF₃ LbL assemblies for three samples: a) [PSS] = 0.5 g/L and 20 CeF₃ for each SiO₂ core (panel a), b) [PSS] = 2.0 g/L and 20 CeF₃ for each SiO₂ core (panel b), c) [PSS] = 2.0 g/L and 50 CeF₃ for each SiO₂ core (panel c).

In all three cases, particle adsorption took place in absence of NaCl in the suspension.

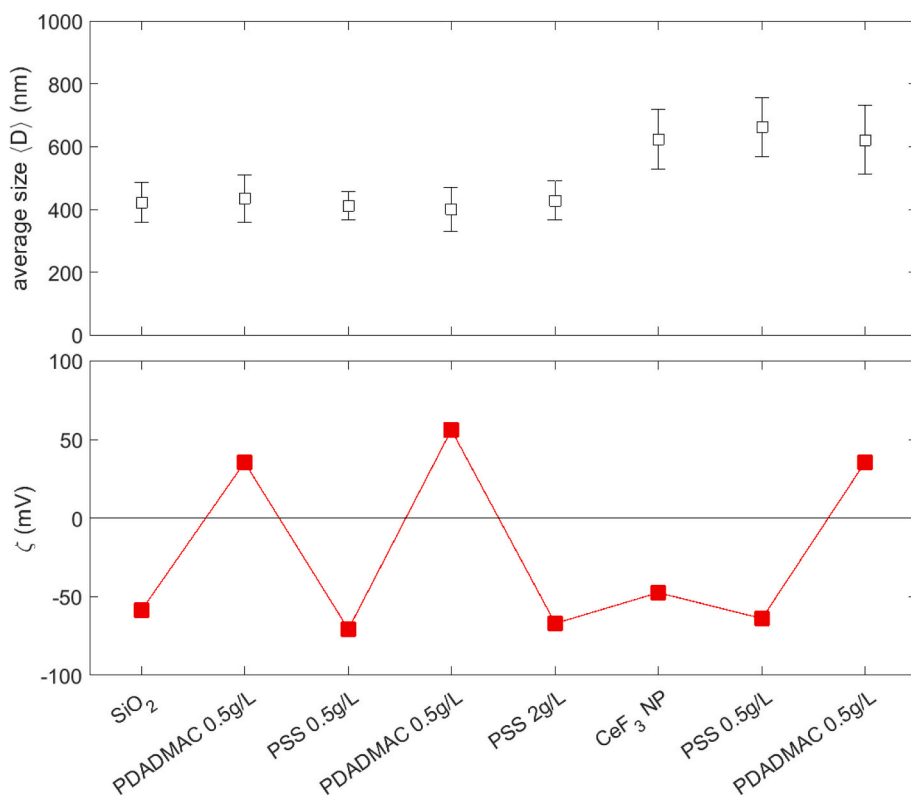


Fig. 3. Size and ζ -potential of the CeF₃ - SiO₂ assembly, as a function of the adsorbed layer. The sample shown here has concentration [PSS] = 2 g/L in the fourth layer and CeF₃:SiO₂ ratio of 50:1. Two additional polyelectrolyte LbL layers are added after the CeF₃ NP layer. Top: average size, computed as the first moment of the volume-weighted diameter distribution obtained by CONTIN analysis of DLS measurements. Error bars are Half Width at Half Maximum (HWHM) of the same distribution. Bottom: ζ -potential. The adsorption of CeF₃ nanoparticles leads to the formation of an incomplete layer, indicated by the negative value of ζ -potential despite the value $+53 \pm 1$ mV measured in CeF₃ NP suspension.

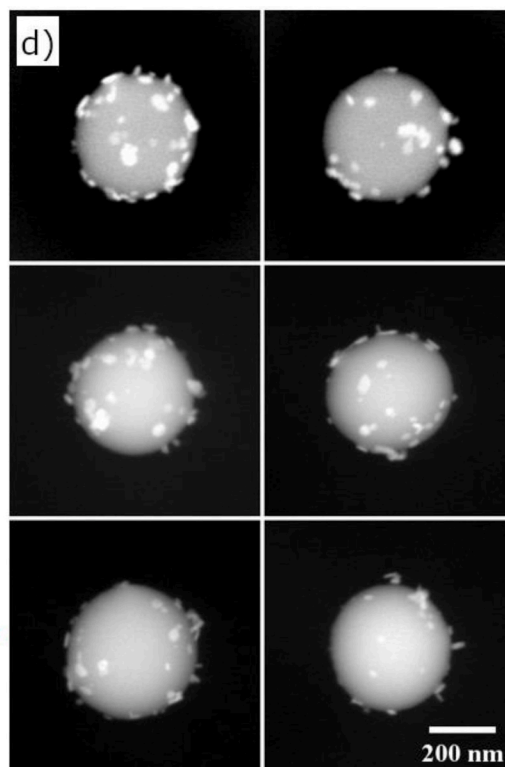
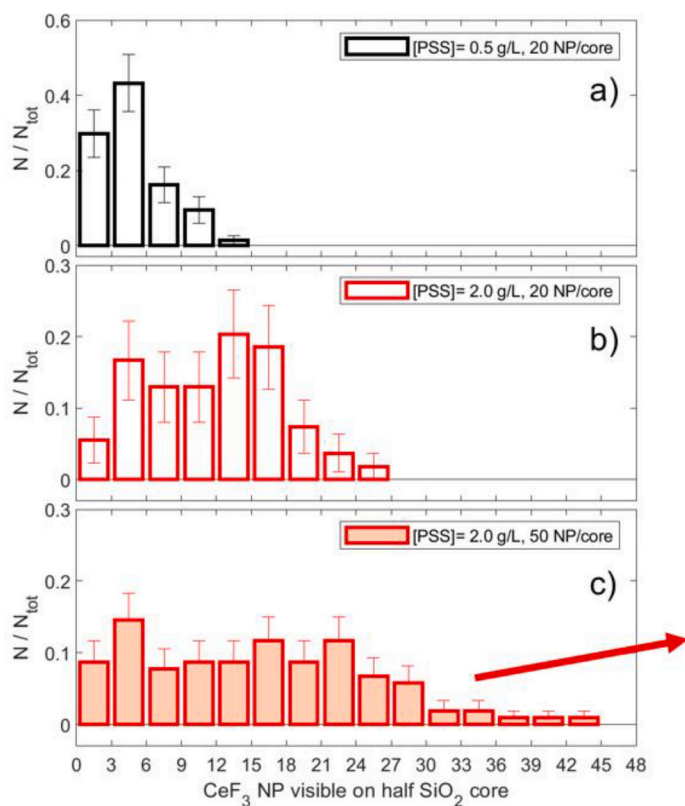


Fig. 4. a-c: Histograms of the number of CeF₃ NP adsorbed on the visible half of SiO₂-CeF₃ assemblies in a SEM micrograph (bars). Error bars are the square root of the number N of occurrences. a) [PSS] = 0.5 g/L and 20 CeF₃ per SiO₂; b) [PSS] = 2.0 g/L and 20 CeF₃ per SiO₂; c) [PSS] = 2.0 g/L and 50 CeF₃ per SiO₂. d) selection of SEM micrograph of SiO₂-CeF₃ assemblies for [PSS] = 2 g/L, 50 CeF₃ per SiO₂. As supplementary information, we report a collection of 48 assemblies used for histogram b).

The effect of [NaCl] has also been investigated; it is reported as Supplementary Information. Briefly, we find that the higher adsorption of CeF_3 NP is achieved when no salt is added to the suspension; moreover, the presence of salt up to 30 mM leads to the formation of micrometre-sized aggregates of SiO_2 NP detected by DLS measurements.

The SEM, DLS and ζ -potential characterization demonstrate that this electrostatic adsorption procedure allows us to adsorb known amount of CeF_3 NP on the SiO_2 cores, avoiding the formation of micrometre-sized CeF_3 - SiO_2 aggregates, with marginal amounts of CeF_3 NP as free particles within the suspension.

3.3. Electrostatic adsorption of CeF_3 and ZnO nanoparticles on SiO_2 cores

The insight gained from the investigation of the electrostatic adsorption process of CeF_3 NP was used to build assemblies that have both CeF_3 and ZnO NP within the polyelectrolyte shell, and to test the formation of multiple nanoparticle layers.

ZnO NP and CeF_3 NP have similar size and ζ -potential on average, as reported in Section 2.4. Following the same procedure described in the previous section, we adsorbed two mixed CeF_3 -ZnO NP layers with ratio 25 CeF_3 + 25 ZnO: 1 SiO_2 , and a third NP layer contained only ZnO particles with ratio 50 ZnO: 1 SiO_2 .

DLS and ζ -potential results are reported in Fig. 5. The average diameter is computed as the first moment of the volume-weighted distribution obtained by the CONTIN algorithm; it increases by 100–150 nm every time a NP layer is added, with a slight increase of the distribution Full Width at Half Maximum. We observe fluctuations of the average size when polyelectrolyte layers are added after a NP layer. We attribute this to the gentle shaking performed with a vortex shaker, instead of sonication as in [28], that we choose to use to disperse the particulate after every centrifugation-washing step. This choice is dictated by the need to avoid possible damage to the nanostructures due to desorption of adsorbed NP.

SEM and EDS spectroscopy have been used to test the adsorption of CeF_3 and ZnO nanoparticle. Fig. 6 reports the EDS characterization of an assembly, with EDS maps (panels b-d) and spectra (panel e) confirming the presence of both CeF_3 and ZnO NP within the polyelectrolyte shell. As Supplementary Information we provide a collection of SEM micrographs of such nanostructures (fig. S4). The phase purity of ZnO and CeF_3 nanocrystals was confirmed by High Resolution Transmission Electron Microscopy (HR-TEM); results are reported as panels f and g of Fig. 6.

The presence of CeF_3 and ZnO within the sample is also confirmed by the fluorescence spectra shown in Fig. 7. The top panel reports the spectra measured on the SiO_2 cores (grey) and on the assembly containing CeF_3 and ZnO NP (red). Emission spectra are reported as solid lines, excitation spectra as dash-dot lines. The difference between the two curves, calculated to highlight the contribution of CeF_3 and ZnO NP alone, is reported in the bottom panel. The emission spectrum presents the broad emission band of CeF_3 at 300 nm, as well as the emission band in the green-yellow region, 550 nm–620 nm, characteristic of ZnO NP [18]. The excitation spectrum presents an excitation peak at 150 nm, characteristic of CeF_3 nanoparticles. The emission spectrum of CeF_3 and ZnO are an indirect evidence that the realized nanostructure will exhibit XPDT functionality, in analogy with similar nanostructures already well characterized by us [18,19].

3.4. Towards the application as XPDT agents

The combination of CeF_3 and ZnO nanoparticles for application in XPDT has been investigated in several papers in the literature, starting from the seminal paper by the group lead by prof Chen Wei at University of Texas, which first demonstrated that CeF_3 scintillating nanoparticles act as an energy mediator between an X-ray beam and ZnO [20]. Previously, we reported on the cytocompatibility, internalization and XPDT functionality of SiC/SiO_x core shell nanowires and of CeF_3 -ZnO

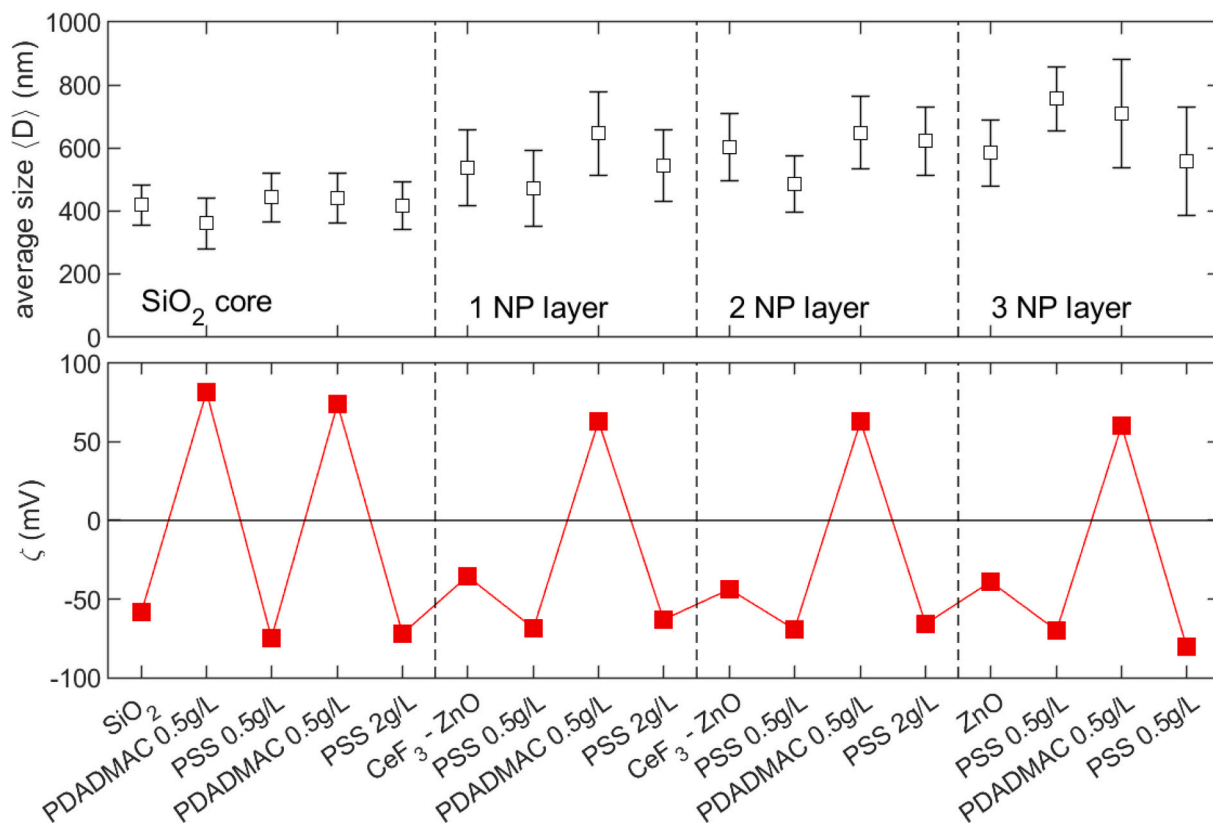


Fig. 5. Size and ζ -potential of CeF_3 - ZnO - SiO_2 assemblies, as a function of the adsorbed layer. Top: average size computed as the first moment of the volume-weighted diameter distribution obtained by CONTIN analysis of DLS measurements. Error bars are HWHM of the same distribution. Bottom: ζ -potential.

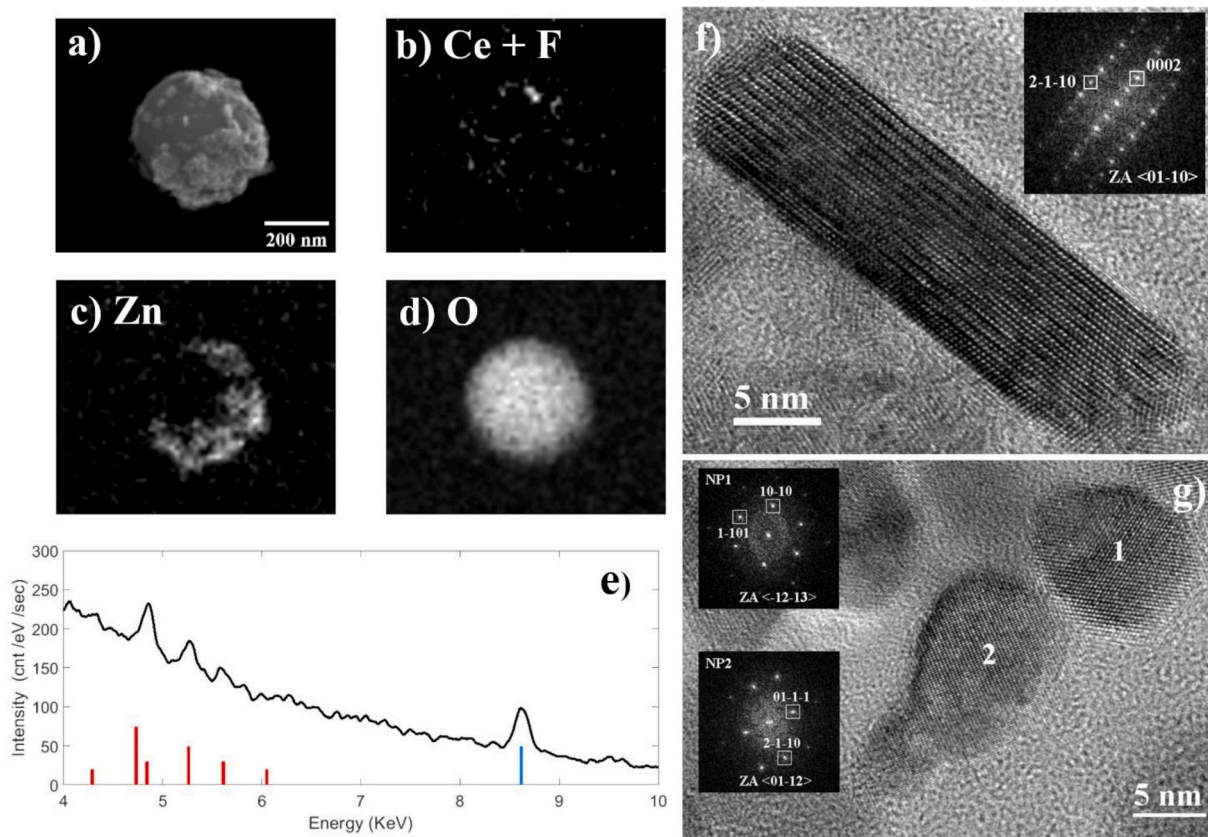


Fig. 6. SEM-EDS analysis of a CeF_3 -ZnO-SiO₂ assembly. a) SEM micrograph, taken with the Secondary Electron detector. b-d) EDS maps, recorded at electron beam energy of 12 keV, for elements b) Ce and F, c) Zn, d) O. EDS maps are sums of three maps of duration 180 s, re-aligned manually. A gaussian filter with sigma = 0.5pixel has been applied. e) EDS spectrum measured at 12 keV excitation, integrating over the whole nanostructure. Red lines indicate the L X-ray emission lines of Ce atoms, the blue line indicates the $\text{K}\alpha_1$ emission lines of Zn atoms. f-g) Zero-loss filtered high resolution TEM images, showing the crystalline structure of CeF_3 (f) and ZnO (g) nanoparticles. The corresponding diffractograms are shown as insets, with the indication of the viewing direction (Zone Axis, ZA). The experimentally measured lattice spacings and angles between different directions match well those of hexagonal CeF_3 (JCPDS card 8-45) and hexagonal ZnO (JCPDS card 36-1451). (For interpretation of the references to colour in this figure legend, the reader is referred to the web version of this article.)

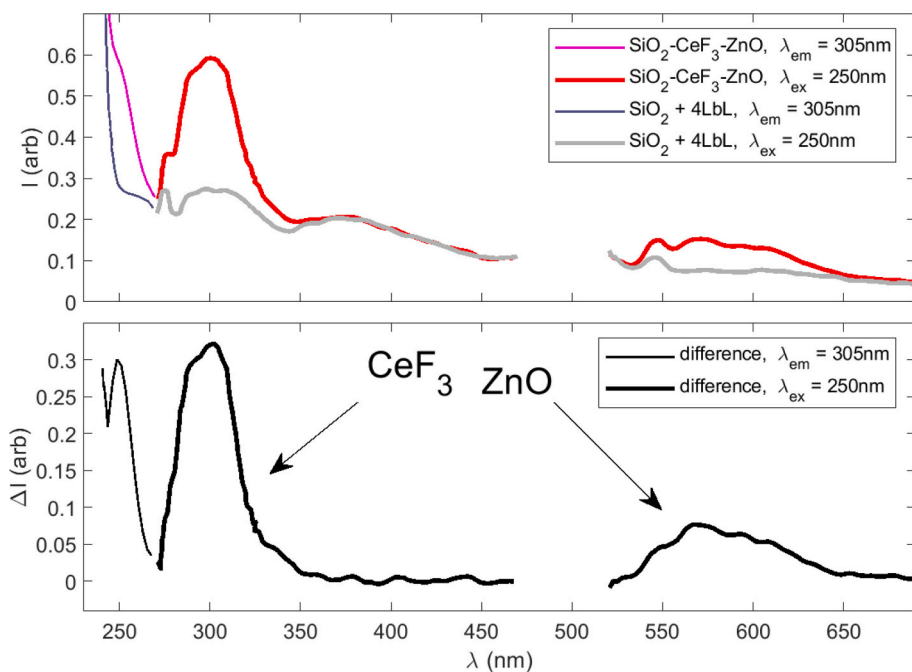


Fig. 7. top) Luminescence spectra recorded on the SiO₂ cores (grey) and on the assembly containing CeF_3 and ZnO NP (red). Thick lines are emission spectra with excitation wavelength 250 nm. Thin lines are excitation spectra with emission wavelength 305 nm. bottom) difference of the spectra of the top panel. The broad band centred at 300 nm is characteristic of CeF_3 NP, while the broad band at 550–620 nm is characteristic of ZnO. The interval between 470 and 520 nm was omitted, as it contains the second order diffraction of the excitation line. (For interpretation of the references to colour in this figure legend, the reader is referred to the web version of this article.)

nanostructures in A549 cells [17–19]. In particular, CeF_3 -ZnO nanostructures with size in the range 100–500 nm showed no appreciable cytotoxicity after 72 h on human adenocarcinoma (A549) cells for concentrations up to 50 $\mu\text{g/mL}$ [18]. Viability of A549 cells was significantly reduced when cells incubated with these nanostructures are irradiated by a 6 MeV X-ray beam from an hospital-grade accelerator (1.2 Gy) [19]. The size of such nanostructures does not impair XPDT functionality.

As a preliminary test of the XPDT performances of these new structures, we measured the efficiency of generation of singlet oxygen (quantum yield Φ) under irradiation with a UV laboratory source ($\lambda = 254 \text{ nm}$); this test has proved successful in predicting also singlet oxygen generation under irradiation with X-rays from a Radiotherapy source [19]. We used the chemofluorescent probe Singlet Oxygen Sensor Green (SOSG) following the methodology detailed in [19,36]. Results for a 50 $\mu\text{g/mL}$ suspension of CeF_3 and ZnO nanoparticles are reported in Fig. 8; the number of generated $^1\text{O}_2$ species is reported as a function of photons incident on the sample. Linear proportionality is evident, as indicated by the dashed line in the figure. By linear fitting, we obtain the $^1\text{O}_2$ quantum yield $\Phi = 0.35 \pm 11$.

The preliminary assessment of the performances of these nanostructures have to be considered in comparison with other recently developed XPDT nanostructures that relies on electrostatic adsorption, such as nanostructures based on mesoporous silica and loaded with molecular photosensitizers, which show comparable singlet oxygen generation in preliminary assays. For instance, Eu-doped scintillating nanoparticles coated by mesoporous silica and loaded with merocyanine 540 suppress tumour growth in mice under 70KeV irradiation [41]. Ti-doped mesoporous silica nanoparticles (MSN) loaded with Protoporphyrin IX showed an enhanced reduction in viability of HT-29 (colorectal adenocarcinoma) cells under 0.1 Gy, 6 MeV irradiation [42]. A lanthanide-doped core–shell–shell scintillating nanocomposite, coated by mesoporous silica and then coated by a poly(allylamine) – Rose Bengal - Polyethylene glycol LbL multilayer, showed a 20% viability reduction observed in MDA-MB-231 and MCF-7 human breast cancer cells under 1 Gy X-ray irradiation [43].

Recently, promising results were shown by new self-assembled nanostructures for XPDT based on micelles and liposomes.

Polyethylene glycol – bilirubin micelles encapsulating scintillating CaWO_4 nanoparticles with size 200 nm showed 90% mortality observed on HN31 (pharyngeal cancer) cells [44]. Liposomes with verteporfin withing the bilayer and containing gold NP caused a 50% viability reduction in HCT116 (colon carcinoma) cells through mitochondrial damage when irradiated with 4 Gy, 320 KeV X-rays [45].

4. Conclusions

We reported the rationale development of a nanostructure with X-ray induced Photodynamic Therapy (XPDT) capability. XPDT nanoparticles are embedded by electrostatic adsorption within a polyelectrolyte shell assembled around the SiO_2 core, formed using the Layer-by-Layer technique. The logical design strategy ensures narrow size distribution and control of the concentration of XPDT agents within the shell.

Optimal experimental parameters of the electrostatic adsorption process - such as the number of polyelectrolyte layers, the concentration of the polyelectrolyte solution during the adsorption process, the maximum surface density of adsorbed XPDT NP - were determined by an investigation on planar silicon substrate, performed using a combination of null-ellipsometry and Scanning Electron Microscopy. Uniform, homogeneous multilayers were obtained with 4 polyelectrolyte layers around the core. A maximum value of the surface density of CeF_3 NP, equal to 50 $\text{particles}/\mu\text{m}^2$, was obtained when they are adsorbed in absence of NaCl, on a PSS layer previously formed from a solution with concentration [PSS] = 2 g/L and 15 mM NaCl."

Building on this information, we applied an analogous procedure on SiO_2 NP cores with average diameter 420 nm. The amount of XPDT nanoparticles added to the suspension is calculated from the surface density of adsorbed particles determined in planar geometry. This ensured their complete adsorption around the SiO_2 core, minimizing the amount of "free" XPDT NP within the suspension; also, this eliminates the need of a separation step to eliminate a possible excess, which would be challenging due to the small difference in size between XPDT NP and SiO_2 NP. The adsorption process was monitored by Dynamic Light Scattering and ζ -potential analysis. Analysis of SEM micrographs was used to characterize the distribution of number of XPDT NP on SiO_2 cores, as a function of the composition of the outer polyelectrolyte layer

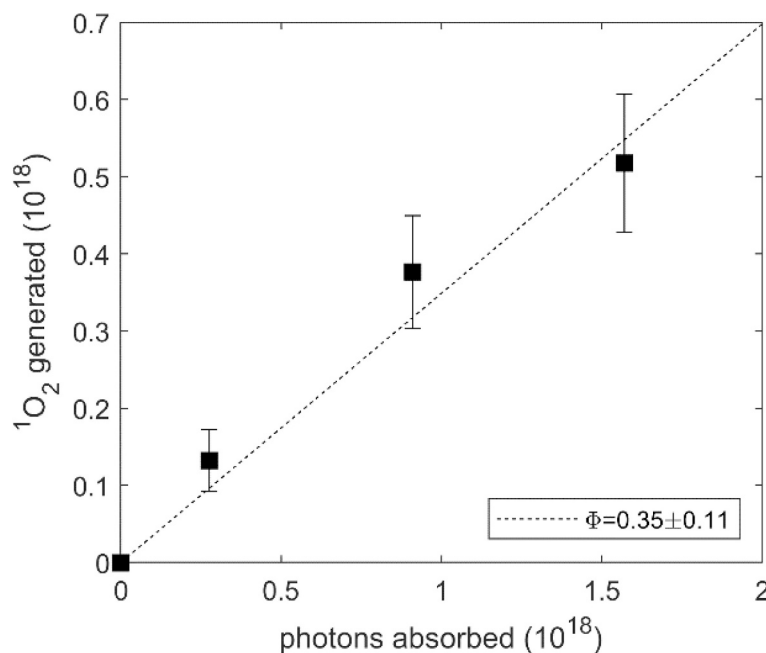


Fig. 8. Efficiency of singlet oxygen generation by CeF_3 -ZnO nanoparticles under UV irradiation ($\lambda = 254 \text{ nm}$). The number of generated $^1\text{O}_2$ species, detected by the SOSG chemofluorescent probe, is measured as a function of absorbed photons, following the methodology detailed in [19,36]. Linear proportionality is evident (dashed line). From its slope, the yield $\Phi = 0.35 \pm 0.11$ is estimated.

and of the ionic strength.

Having optimized the electrostatic adsorption process of CeF₃ and ZnO NP around SiO₂ cores, we repeated it three times; after each NP adsorption step, a PSS-PDADMAC-PSS LbL multilayer was built around the assembly. An outer PSS-PDADMAC LbL multilayer encloses the nanostructure. The presence of both CeF₃ and ZnO NP within the nanostructures is confirmed by EDS spectroscopy on individual nanostructures and by Fluorescence spectroscopy on the nanostructure suspension.

Nanostructures combining CeF₃ and ZnO nanoparticles are known as effective XPDT agents on human adenocarcinoma (A549) cancer cells; for instance, under low-dose irradiation with 6 MeV X-rays from a Radiotherapy hospital-grade source, we found a reduction of viability of 18% with a 2 Gy dose with respect to irradiated controls [19]. The detailed characterization reported in this work completes the preliminary steps that are propaedeutic to a characterization of the XPDT performances of these nanostructures *in vitro* and *in vivo*.

Author statement

C.L., O.D. and S.K. planned the experiments. O.D., B.D. and G.G. synthesized and characterized the nanostructures, O.D., B.D. and S. K. performed the LbL growth and characterizations, R.F. performed the HRTEM characterizations, C.L. and D.O. wrote the manuscript. All the authors commented the manuscript.

Declaration of Competing Interest

The authors declare that they have no known competing financial interests or personal relationships that could have appeared to influence the work reported in this paper.

Acknowledgements

We acknowledge prof. Piotr Warszynski for useful discussions. D.B. acknowledges the Erasmus+ program for financial support within a Student Mobility Traineeship (SMT) exchange with the Polish Academy of Sciences. D.O. acknowledges financial support by the Programme “FIL-Quota Incentivante” of University of Parma, co-sponsored by Fondazione Cariparma.

Appendix A. Supplementary data

Supplementary data to this article can be found online at <https://doi.org/10.1016/j.colcom.2020.100327>.

References

- [1] K. Otto, Volumetric modulated arc therapy: IMRT in a single gantry arc, *Med. Phys.* 35 (2008) 310–317, <https://doi.org/10.1118/1.2818738>.
- [2] M. Teoh, C.H. Clark, K. Wood, S. Whitaker, A. Nisbet, Volumetric modulated arc therapy: a review of current literature and clinical use in practice, *Br. J. Radiol.* 84 (2011) 967–996, <https://doi.org/10.1259/bjr/22373346>.
- [3] C.-M. Hu, L. Zhang, Therapeutic nanoparticles to combat Cancer drug resistance, *Curr. Drug Metab.* 10 (2010) 836–841, <https://doi.org/10.2174/138920009790274540>.
- [4] A. Shapira, Y.D. Livney, H.J. Broxterman, Y.G. Assaraf, Nanomedicine for targeted cancer therapy: towards the overcoming of drug resistance, *Drug Resist. Updat.* 14 (2011) 150–163, <https://doi.org/10.1016/j.drup.2011.01.003>.
- [5] A. Hervault, A.E. Dunn, M. Lim, C. Boyer, D. Mott, S. Maenosono, N.T.K. Thanh, Doxorubicin loaded dual pH- and thermo-responsive magnetic nanocarrier for combined magnetic hyperthermia and targeted controlled drug delivery applications, *Nanoscale* 8 (2016) 12152–12161, <https://doi.org/10.1039/C5NR07773G>.
- [6] V. Zamora-Mora, M. Fernández-Gutiérrez, Á. González-Gómez, B. Sanz, J. S. Román, G.F. Goya, R. Hernández, C. Mijangos, Chitosan nanoparticles for combined drug delivery and magnetic hyperthermia: from preparation to *in vitro* studies, *Carbohydr. Polym.* 157 (2017) 361–370, <https://doi.org/10.1016/j.carbpol.2016.09.084>.
- [7] W. Xie, Q. Gao, Z. Guo, D. Wang, F. Gao, X. Wang, Y. Wei, L. Zhao, Injectable and self-healing thermosensitive magnetic hydrogel for asynchronous control release of doxorubicin and docetaxel to treat triple-negative breast cancer, *ACS Appl. Mater. Interfaces* 9 (2017) 33660–33673, <https://doi.org/10.1021/acsami.7b10699>.
- [8] L. Cristofolini, K. Szczepanowicz, D. Orsi, T. Rimoldi, F. Albertini, P. Warszynski, Hybrid polyelectrolyte/Fe₃O₄ nanocapsules for hyperthermia applications, *ACS Appl. Mater. Interfaces* 8 (2016) 25043–25050, <https://doi.org/10.1021/acsami.6b05917>.
- [9] Z. Guo, K. Zheng, Z. Tan, Y. Liu, Z. Zhao, G. Zhu, K. Ma, C. Cui, L. Wang, T. Kang, Overcoming drug resistance with functional mesoporous titanium dioxide nanoparticles combining targeting, drug delivery and photodynamic therapy, *J. Mater. Chem. B* 6 (2018) 7750–7759, <https://doi.org/10.1039/c8tb01810c>.
- [10] B. Poinard, S.Z.Y. Neo, E.L.L. Yeo, H.P.S. Heng, K.G. Neoh, J.C.Y. Kah, Polydopamine nanoparticles enhance drug release for combined photodynamic and photothermal therapy, *ACS Appl. Mater. Interfaces* 10 (2018) 21125–21136, <https://doi.org/10.1021/acsami.8b04799>.
- [11] M. Gary-Boho, O. Hocine, D. Brevet, M. Maynadier, L. Raehm, S. Richeter, V. Charasson, B. Looock, A. Morère, P. Maillard, M. Garcia, J.O. Durand, Cancer therapy improvement with mesoporous silica nanoparticles combining targeting, drug delivery and PDT, *Int. J. Pharm.* 423 (2012) 509–515, <https://doi.org/10.1016/j.ijpharm.2011.11.045>.
- [12] W. Chen, J. Zhang, Using nanoparticles to enable simultaneous radiation and photodynamic therapies for cancer treatment, *J. Nanosci. Nanotechnol.* 6 (2006) 1159–1166, <https://doi.org/10.1166/jnn.2006.327>.
- [13] J. Chen, T. Fan, Z. Xie, Q. Zeng, P. Xue, T. Zheng, Y. Chen, X. Luo, H. Zhang, Advances in nanomaterials for photodynamic therapy applications: status and challenges, *Biomaterials* 237 (2020) 119827, <https://doi.org/10.1016/j.biomaterials.2020.119827>.
- [14] Z. Gadzhimagomedova, P. Zolotukhin, O. Kit, D. Kirsanova, A. Soldatov, Nanocomposites for X-ray photodynamic therapy, *Int. J. Mol. Sci.* 21 (2020) 4004, <https://doi.org/10.3390/ijms21114004>.
- [15] M. Sivasubramanian, Y. Chuang, L.-W. Lo, Evolution of nanoparticle-mediated photodynamic therapy: from superficial to deep-seated cancers, *Molecules* 24 (2019) 520, <https://doi.org/10.3390/molecules24030520>.
- [16] M. Overchuk, M.H.Y. Cheng, G. Zheng, X-ray-activatable photodynamic nanoconstructs, *ACS Cent. Sci.* 6 (2020) 613–615, <https://doi.org/10.1021/acscentsci.0c00303>.
- [17] F. Rossi, E. Bedogni, F. Bigi, T. Rimoldi, L. Cristofolini, S. Pinelli, R. Alinovi, M. Negri, S.C. Dhanabalan, G. Attolini, F. Fabbri, M. Goldoni, A. Mutti, G. Benecchi, C. Ghetti, S. Iannotta, G. Salviati, Porphyrin conjugated SiC/SiOx nanowires for X-ray-excited photodynamic therapy, *Sci. Rep.* 5 (2015) 7606, <https://doi.org/10.1038/srep07606>.
- [18] T. Rimoldi, D. Orsi, P. Lagonegro, B. Ghezzi, C. Galli, F. Rossi, G. Salviati, L. Cristofolini, CeF₃-ZnO scintillating nanocomposite for self-lighted photodynamic therapy of cancer, *J. Mater. Sci. Mater. Med.* 27 (2016) 159, <https://doi.org/10.1007/s10856-016-5769-3>.
- [19] D. Orsi, T. Rimoldi, S. Pinelli, R. Alinovi, M. Goldoni, G. Benecchi, F. Rossi, L. Cristofolini, New CeF₃-ZnO nanocomposites for self-lighted photodynamic therapy that block adenocarcinoma cell life cycle, *Nanomedicine* 13 (2018) 2311–2326, <https://doi.org/10.2217/nnm-2017-0399>.
- [20] S. Sahi, W. Chen, Luminescence enhancement in CeF₃/ZnO nanocomposites for radiation detection, *Radiat. Meas.* 59 (2013), <https://doi.org/10.1016/j.radmeas.2013.04.015>.
- [21] Y. Huang, F. Qiu, R. Chen, D. Yan, X. Zhu, Fluorescence resonance energy transfer-based drug delivery systems for enhanced photodynamic therapy, *J. Mater. Chem. B* 8 (2020) 3772–3788, <https://doi.org/10.1039/d0tb00262c>.
- [22] C. Yi, Z. Yu, Q. Ren, X. Liu, Y. Wang, X. Sun, S. Yin, J. Pan, X. Huang, Nanoscale ZnO-based photosensitizers for photodynamic therapy, *Photodiagn. Photodyn. Ther.* 30 (2020) 101694, <https://doi.org/10.1016/j.pdpdt.2020.101694>.
- [23] G. Decher, Fuzzy nanoassemblies: toward layered polymeric multicomposites, *Science* 80 (277) (1997) 1232–1237, <https://doi.org/10.1126/science.277.5330.1232>.
- [24] J.J. Richardson, M. Björnalm, F. Caruso, Technology-driven layer-by-layer assembly of nanofilms, *Science* 80 (348) (2015), <https://doi.org/10.1126/science.aaa2491>.
- [25] E. Guzmán, R.G. Rubio, F. Ortega, A closer physico-chemical look to the Layer-by-Layer electrostatic self-assembly of polyelectrolyte multilayers, *Adv. Colloid Interf. Sci.* 282 (2020), <https://doi.org/10.1016/j.cis.2020.102197>.
- [26] W. Sun, T. Shi, L. Luo, X. Chen, P. Lv, Y. Lv, Y. Zhuang, J. Zhu, G. Liu, X. Chen, H. Chen, Monodisperse and uniform mesoporous silicate nanosensitizers achieve low-dose X-ray-induced deep-penetrating photodynamic therapy, *Adv. Mater.* 31 (2019) 1–8, <https://doi.org/10.1002/adma.201808024>.
- [27] N. Raghunand, R.J. Gillies, pH and drug resistance in tumors, *Drug Resist. Updat.* 3 (2000) 39–47, <https://doi.org/10.1054/drup.2000.0119>.
- [28] F. Caruso, H. Möhwald, Preparation and characterization of ordered nanoparticle and polymer composite multilayers on colloids, *Langmuir* 15 (1999) 8276–8281, <https://doi.org/10.1021/la990426v>.
- [29] T. Bollhorst, K. Rezwani, M. Maas, Colloidal capsules: nano- and microcapsules with colloidal particle shells, *Chem. Soc. Rev.* 46 (2017) 2091–2126, <https://doi.org/10.1039/c6cs00632a>.
- [30] X.W. Lou, L.A. Archer, Z. Yang, Hollow micro-/nanostructures: synthesis and applications, *Adv. Mater.* 20 (2008) 3987–4019, <https://doi.org/10.1002/adma.200800854>.
- [31] G.H. Bogush, M.A. Tracy, C.F. Zukoski, Preparation of monodisperse silica particles: control of size and mass fraction, *J. Non-Cryst. Solids* 104 (1988) 95–106, [https://doi.org/10.1016/0022-3093\(88\)90187-1](https://doi.org/10.1016/0022-3093(88)90187-1).
- [32] C. Li, F. Li, T. Li, T. Bai, L. Wang, Z. Shi, S. Feng, A facile synthesis and photoluminescence properties of water-dispersible Re³⁺ doped CeF₃ nanocrystals

- and solid nanocomposites with polymers, *Dalton Trans.* 41 (2012) 4890–4895, <https://doi.org/10.1039/c2dt30064h>.
- [33] S. Erokhina, T. Berzina, L. Cristofolini, V. Erokhin, C. Folli, O. Konovalov, I.-G. Marino, M.P. Fontana, X-ray reflectivity measurements of layer-by-layer films at the solid/liquid interface, *Langmuir* 24 (2008) 12093–12096, <https://doi.org/10.1021/la802060e>.
- [34] R. M. A Azzam, N.M. Bashara. *Ellipsometry and Polarized Light*, North-Holland Pub. Co, Amsterdam, 1977.
- [35] M. Harke, R. Teppner, O. Schulz, H. Motschmann, H. Orendi, Description of a single modular optical setup for ellipsometry, surface plasmons, waveguide modes, and their corresponding imaging techniques including Brewster angle microscopy, *Rev. Sci. Instrum.* 68 (1997) 3130–3134, <https://doi.org/10.1063/1.1148256>.
- [36] S. Clement, W. Deng, E. Camilleri, B.C. Wilson, E.M. Goldys, X-ray induced singlet oxygen generation by nanoparticle-photosensitizer conjugates for photodynamic therapy: determination of singlet oxygen quantum yield, *Sci. Rep.* 6 (2016) 19954, <https://doi.org/10.1038/srep19954>.
- [37] R. Monchaux, M. Bourgoïn, A. Cartellier, Preferential concentration of heavy particles: a Voronoï analysis, *Phys. Fluids* 22 (2010), <https://doi.org/10.1063/1.3489987>.
- [38] M. Ferraro, L. Zaninetti, On the statistics of area size in two-dimensional thick Voronoi diagrams, *Phys. A Stat. Mech. Appl.* 391 (2012) 4575–4582, <https://doi.org/10.1016/j.physa.2012.05.029>.
- [39] E. Guzmán, H.A. Ritacco, F. Ortega, R.G. Rubio, Growth of polyelectrolyte layers formed by poly(4-styrenesulfonate sodium salt) and two different polycations: new insights from study of adsorption kinetics, *J. Phys. Chem. C* 116 (2012) 15474–15483, <https://doi.org/10.1021/jp304522t>.
- [40] E. Guzmán, H. Ritacco, F. Ortega, R.G. Rubio, Evidence of the influence of adsorption kinetics on the internal reorganization of polyelectrolyte multilayers, *Colloids Surf. A Physicochem. Eng. Asp.* 384 (2011) 274–281, <https://doi.org/10.1016/j.colsurfa.2011.04.005>.
- [41] H. Chen, G.D. Wang, Y.-J. Chuang, Z. Zhen, X. Chen, P. Biddinger, Z. Hao, F. Liu, B. Shen, Z. Pan, J. Xie, Nanoscintillator-mediated X-ray inducible photodynamic therapy for in vivo cancer treatment, *Nano Lett.* 15 (2015) 2249–2256, <https://doi.org/10.1021/nl504044p>.
- [42] A. Vejdani Noghreiyani, M.R. Sazegar, S.A. Mousavi Shaegh, A. Sazgarnia, Investigation of the emission spectra and cytotoxicity of TiO₂ and Ti-MSN/PpIX nanoparticles to induce photodynamic effects using X-ray, *Photodiagn. Photodyn. Ther.* 30 (2020) 101770, <https://doi.org/10.1016/j.pdpdt.2020.101770>.
- [43] C.C. Hsu, S.L. Lin, C.A. Chang, Lanthanide-doped core-shell-Shell nanocomposite for dual photodynamic therapy and luminescence imaging by a single X-ray excitation source, *ACS Appl. Mater. Interfaces* 10 (2018) 7859–7870, <https://doi.org/10.1021/acsami.8b00015>.
- [44] V.J. Pizzuti, D. Viswanath, S.E. Torregrosa-Allen, M.P. Currie, B.D. Elzey, Y. Won, Bilirubin-coated radioluminescent particles for radiation-induced photodynamic therapy, *ACS Appl. Bio Mater.* 3 (2020) 4858–4872, <https://doi.org/10.1021/acsabm.0c00354>.
- [45] X. Gu, X. Gu, X. Gu, C. Shen, H. Li, E.M. Goldys, W. Deng, X-ray induced photodynamic therapy (PDT) with a mitochondria-targeted liposome delivery system, *J. Nanobiotechnol.* 18 (2020) 1–13, <https://doi.org/10.1186/s12951-020-00644-z>.